The Astrophysical Journal Letters, 980:L44 (13pp), 2025 February 20 https://doi.org/10.3847/2041-8213/adade6

SN 2023zaw: The Low-energy Explosion of an Ultrastripped Star

T. Moore[1,2], J. H. Gillanders[3], M. Nicholl[1], M. E. Huber[4], S. J. Smartt[1,3], S. Srivastav[3], H. F. Stevance[1,3,5], T.-W. Chen[6], K. C. Chambers[4], J. P. Anderson[2,7], M. D. Fulton[1], S. R. Oates[8], C. Angus[1], G. Pignata[9], N. Erasmus[10,11], H. Gao[4], J. Herman[4], C.-C. Lin[4], T. Lowe[12], E. A. Magnier[12], P. Minguez[12], C.-C. Ngeow[6], X. Sheng[1], S. A. Sim[1], K. W. Smith[1], R. Wainscoat[12], S. Yang[13], D. R. Young[1], and K.-J. Zeng[6]
[1] Astrophysics Research Centre, School of Mathematics and Physics, Queen's University Belfast, BT7 1NN, UK; tmoore11@qub.ac.uk
[2] European Southern Observatory, Alonso de Córdova 3107, Casilla 19, Santiago, Chile
[3] Astrophysics sub-Department, Department of Physics, University of Oxford, Keble Road, Oxford, OX1 3RH, UK
[4] Institute for Astronomy, University of Hawai'i, 2680 Woodlawn Drive, Honolulu, HI 96822, USA
[5] Department of Physics, The University of Auckland, Private Bag 92019, Auckland, New Zealand
[6] Graduate Institute of Astronomy, National Central University, 300 Jhongda Road, 32001 Jhongli, Taiwan
[7] Millennium Institute of Astrophysics (MAS), Nuncio Monseñor Sótero Sanz 100, Providencia, Santiago, Chile
[8] Department of Physics, Lancaster University, Lancaster, LA1 4YB, UK
[9] Instituto de Alta Investigación, Universidad de Tarapacá, Arica, Casilla 7D, Chile
[10] South African Astronomical Observatory, PO Box 9, Observatory 7935, Cape Town, South Africa
[11] Department of Physics, Stellenbosch University, Stellenbosch, 7602, South Africa
[12] Institute for Astronomy, University of Hawaii, 2680 Woodlawn Drive, Honolulu, HI 96822, USA
[13] Henan Academy of Sciences, Zhengzhou 450046, Henan, People's Republic of China

Received 2024 May 21; revised 2025 January 17; accepted 2025 January 20; published 2025 February 19

Abstract

Most stripped-envelope supernova progenitors are thought to be formed through binary interaction, losing hydrogen and/or helium from their outer layers. Ultrastripped supernovae are an emerging class of transient that are expected to be produced through envelope stripping by a neutron star companion. However, relatively few examples are known, and the outcomes of such systems can be diverse and are poorly understood at present. Here we present spectroscopic observations and high-cadence, multiband photometry of SN 2023zaw, a rapidly evolving supernova with a low ejecta mass. SN 2023zaw was discovered in a nearby spiral galaxy at $D = 39.7$ Mpc. It has significant Milky Way extinction, $E(B-V)_{\rm MW} = 0.21$, and significant (but uncertain) host extinction. Bayesian evidence comparison reveals that nickel is not the only power source and that an additional energy source is required to explain our observations. Our models suggest that an ejecta mass of $M_{\rm ej} \sim 0.07\,M_\odot$ and a synthesised nickel mass of $M_{\rm Ni} \sim 0.007\,M_\odot$ are required to explain the observations. We find that additional heating from a central engine, or interaction with circumstellar material, can power the early light curve.

Unified Astronomy Thesaurus concepts: Transient sources (1851); Supernovae (1668); Core-collapse supernovae (304); Type Ib supernovae (1729); Circumstellar matter (241)

Materials only available in the online version of record: data behind figure

1. Introduction

Modern sky surveys such as the Asteroid Terrestrial-impact Last Alert System (ATLAS; J. L. Tonry et al. 2018), Zwicky Transient Facility (ZTF; E. C. Bellm et al. 2019), and the Panoramic Survey Telescope and Rapid Response System (Pan-STARRS; K. C. Chambers et al. 2016) are revealing the extremes of core-collapse supernovae (CCSNe) and optical transients (C. Inserra 2019; M. Modjaz et al. 2019). A small number of supernovae (SNe), often belonging to the hydrogen poor Types Ib and Ic, show rapid evolution and brighten and fade on timescales much faster than typical classes of SNe (D. Poznanski et al. 2010; M. R. Drout et al. 2013; K. De et al. 2018; S. J. Prentice et al. 2018; P. Chen et al. 2020; S. J. Prentice et al. 2020; A. Y. Q. Ho et al. 2023; S. Yan et al. 2023). Generally, a small ejecta mass is invoked to explain the rapid evolution of fast transients (T. J. Moriya et al. 2017). A small ejecta mass reduces the photon diffusion timescale, allowing the light curve to peak and begin to decline rapidly. Low ejecta mass interpretations require a physically compatible powering source. Invoking radioactive ^{56}Ni in fast-evolving SNe frequently produces unphysical ejecta mass to nickel mass ratios (S. J. Prentice et al. 2018; P. Chen et al. 2020; J. H. Gillanders et al. 2020; S. J. Prentice et al. 2020). Additional mechanisms have been suggested to boost the luminosity of these SNe, e.g., interaction with circumstellar material, or energy injection from a magnetar (Y. Yao et al. 2020; R. Sawada et al. 2022).

In this Letter we present spectrophotometric follow-up observations of the rapidly evolving SN 2023zaw.[14] Classified as a Type Ib SN, SN 2023zaw rises rapidly to maximum light (<4 days) followed by a similarly fast decline, comparable to the fast-fading Type I SN 2019bkc (P. Chen et al. 2020; S. J. Prentice et al. 2020). We compare a range of physical models by fitting semianalytical models and show that SN 2023zaw cannot be powered solely by ^{56}Ni decay, the normal power source of CCSNe.

2. Discovery and Follow-up

SN 2023zaw was discovered on 2023 December 7 05:34 UTC (MJD 60285.23) by ZTF (E. C. Bellm et al. 2019) and registered on the Transient Name Server at 11:50 UTC

---

[14] While preparing this Letter, another preprint on the same source appeared on the arXiv (K. K. Das et al. 2024).

(J. Sollerman 2023) with the discovery mag $g = 19.34$. All observational phases in this section are quoted in observer-frame days, relative to the ZTF discovery epoch. We independently detected SN 2023zaw in ATLAS data (K. W. Smith et al. 2020) a few hours later at 08:00 UTC as the field visibility moved from California to Hawaii, at mag $o = 18.74$. The transient is offset $8\overset{''}{.}97$N, $19\overset{''}{.}15$W from UGC 03048, a spiral galaxy with a redshift from the NASA Extragalactic Database (NED) of 0.010150 ± 0.000026 (C. M. Springob et al. 2005). From NED the median redshift-independent distance to UGC 03048 is 39.7 Mpc, based on the Tully–Fisher method (R. B. Tully et al. 2013). SN 2023zaw is located on the edge of one of the two prominent arms of UGC 03048. The Milky Way extinction along this line of sight is $A_V = 0.66$ mag (E. F. Schlafly & D. P. Finkbeiner 2011). Na I D lines in the classification spectrum suggest that additional host extinction is significant (D. Poznanski et al. 2012).

Four AstroNotes regarding SN 2023zaw were released on the Transient Name Server[15] (TNS) at the time of discovery, commenting on its early evolution. V. Karambelkar et al. (2023a) highlighted the discovery and fast-fading nature of SN 2023zaw, along with an observation of the transient with NOT/ALFOSC. The Kinder project (M. H. Lee et al. 2023) reported a color-dependent fade using observations performed on the 40 cm SLT at Lulin Observatory, Taiwan. In M. Fulton et al. (2023), we reported the combined ATLAS and ZTF data and highlighted that this source was flagged by our "Fastfinder" filter and annotator on the Lasair broker[16] (K. W. Smith et al. 2019) to find fast-evolving objects in the ZTF public alert stream. Both V. Karambelkar et al. (2023a) and M. Fulton et al. (2023) identified SN 2023zaw as a fast-fading, subluminous and red transient. Spectroscopic observations with Keck (V. Karambelkar et al. 2023b) reported an apparent similarity with the candidate ".Ia" SN 2010X (M. M. Kasliwal et al. 2010). Finally, J. H. Gillanders et al. (2023) classified the object as a Type Ib SN based on observations performed with Gemini-N/GMOS, and this spectrum was immediately made public on the TNS.

2.1. Photometry

Photometry for SN 2023zaw (internal name ATLAS23wuw) was obtained from the ATLAS forced photometry server (L. Shingles et al. 2021) and binned by day. The ATLAS (J. L. Tonry et al. 2018) system is an all-sky survey for potentially dangerous near-Earth objects. ATLAS data are processed using the ATLAS Science Server (K. W. Smith et al. 2020) to search for stationary transients. We obtained measurements in the g and r bands using the Lasair broker (K. W. Smith et al. 2019) and public ZTF stream data.[17]

We triggered follow-up observations with the 1.8 m Pan-STARRS1 telescope on the Haleakala mountain, Hawaii (K. C. Chambers et al. 2016). The Pan-STARRS1 telescope has a 7 $\deg^2$ field of view and features a 1.4 GP camera. High-cadence observations in the *grizy*_P1 bands were taken from +6 to +44 days post-discovery. Optical imaging was triggered with the 2.0 m Liverpool Telescope (LT; I. A. Steele et al. 2004) using IO:O in *riz* bands under program PL23B26 (PI: M. Fulton). Measurements were made by point-spread function (PSF) fitting using SExtractor (E. Bertin & S. Arnouts 1996) with local background subtraction. We observed SN 2023zaw with the 0.4 m SLT telescope as a part of the Kinder project (T. W. Chen et al. 2021) and measured PSF *griz*-band photometry. Three epochs of photometric observations were performed with the GMOS-N instrument at the Gemini North 8.1 m telescope, under program ID GN-2023B-Q-125 (PI: M. Huber). Photometric Gemini observations were obtained at phases of +44 days (*riz* band), +54 days (*riz* band), and +56 days (*ri*band) post-discovery. These observations were bias subtracted and flat field corrected using standard recipes in `DRAGONS` (K. Labrie et al. 2023a, 2023b). We also present three epochs of r-band photometry derived from the acquisition images obtained prior to our spectroscopic observations with GMOS-N (see Section 2.2 for details). Aperture photometry was performed using `PSF` (M. Nicholl et al. 2023) with a small optimized aperture, an encircled energy correction, and local background subtraction. The Ultra-Violet and Optical Telescope (UVOT; P. W. A. Roming et al. 2005) on board the Neil Gehrels Swift Observatory (Swift; N. Gehrels et al. 2004) satellite observed SN 2023zaw. A single *uvm*2 exposure was taken at +6 days and followed up in the *u*, *b*, *v*, *uvw*1, *uvm*2, and *uvw*2 bands at two epochs +8 to +11 days from discovery. The images at each epoch were coadded, and the count rates were obtained from the stacked images using the Swift tool `uvotsource`. To extract the source counts, we used a source aperture of 5″ radius and an aperture of 20″ radius for the background. The source count rates were converted to magnitudes using the UVOT photometric zero-points (T. S. Poole et al. 2008; A. A. Breeveld et al. 2011). All Swift observations are nondetections of the transient.

The Milky Way extinction-corrected light curve of SN 2023zaw is presented in Figure 1 (see Section 3.1 for details of extinction estimation). We also present a pseudobolometric light curve calculated using the public `SUPERBOL` code (see M. Nicholl 2018a, for a description). `SUPERBOL` applies a simple interpolation to the light curve and integrates underneath the observed photometric (*gcroizy*-band) observations. The error bars on L_{bol} after $t = 20$ days are significantly larger than the errors on the individual photometric data points. This accounts for the fact that the spectral energy distribution (SED) is not well sampled in wavelength by the photometry (having only two or three bands) and the uncertainty in the effective temperature is propagated into the bolometric luminosity estimate (see M. Nicholl 2018a for details). All photometry presented in this work has been made available as a machine-readable table.

2.2. Spectroscopy

We observed SN 2023zaw at three different phases with the Gemini North/GMOS-N instrument under program ID GN-2023B-Q-125 (PI: M. Huber). Our three observations were taken at +6, +10, and 28 days post-discovery (corresponding to phases from maximum light of ≈ +4.2, +8.2, and +26.0 days, respectively). All observations were performed using the R400 grating, sampling the ≈4200–9100 Å wavelength range at a spectral resolution of $R \sim 1000$ for the 1″ slit width employed. All three epochs of Gemini observations were reduced using the `DRAGONS` pipeline (K. Labrie et al. 2023a, 2023b) following standard recipes, and the spectra were all flux-calibrated against the same standard star. The

---

[15] https://www.wis-tns.org/object/2023zaw

[16] https://lasair-ztf.lsst.ac.uk

[17] https://lasair-ztf.lsst.ac.uk/objects/ZTF23absbqun

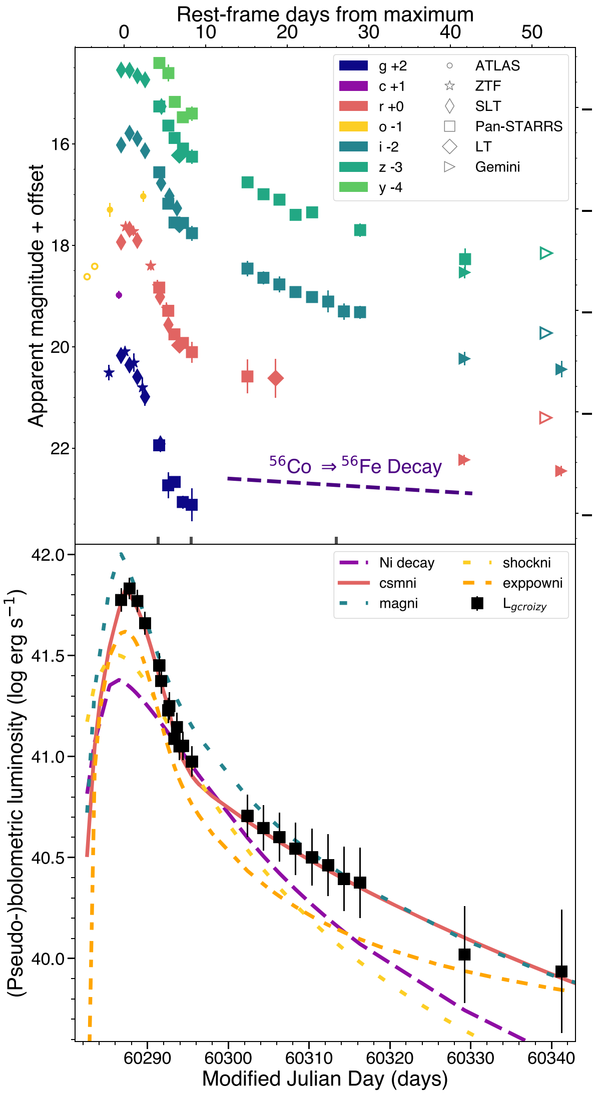

Figure 1. Top: multicolor light curves with corrections for Milky Way foreground extinction and time dilation (for $z = 0.010150$) applied. Each telescope is shown with a different marker, and open markers indicate upper limits. We exclude Swift/UVOT nondetections for visual clarity. Additionally, we show the expected decline rate of a ^{56}Co tail (0.98 mag/100 days; S. E. Woosley et al. 1989). This photometry is available as the data behind the figure. Bottom: a pseudobolometric (*gcroizy*-band) light curve of SN 2023zaw compared to the model light curves from Section 3.3 integrated between the *gcroizy*-band observations. Model light curves are corrected for foreground extinction and the modeling-derived estimate of the host extinction.

(The data used to create this figure are available in the online article.)

contribution of the host galaxy was estimated and subtracted, and each reduced, coadded spectrum agrees well with the background-subtracted Pan-STARRS photometry obtained at the same epoch. All spectra in this work will be made publicly available on the WISeREP repository (O. Yaron & A. Gal-Yam 2012).

3. Analysis

3.1. Host Galaxy and Milky Way Foreground Extinction

There is a strong and narrow absorption line in the +4.2- and +8.2-day GMOS-N spectra, consistent with Na I D absorption at the redshift of UGC 03048. The GMOS-N spectral resolution does not allow the D_1 and D_2 components to be separately measured. After normalizing the spectrum, we fit a single Gaussian to the blended absorption line, finding a center $\lambda_c = 5953.94$ Å ($z = 0.0104$), FWHM = 11.4 Å, and an equivalent width EW = 2.10 ± 0.22 Å. At this redshift, the Na I D lines are separated by 6.03 Å, and the expected instrumental width of a single line is FWHM ≃ 6 Å, giving an expected instrumental width for the unresolved Na I D blend of FWHM ≃ 9 Å.

Measurements of the equivalent width of the Na I doublet have been shown to be correlated with the line-of-sight extinction (D. Poznanski et al. 2012), and this method has often been applied to extragalactic transients. While there is a reasonably linear relation between line strength and $E(B-V)$, up to a total $\mathrm{EW}_{(D_1+D_2)} \simeq 0.7$ Å, the relationship then saturates. No quantitative and unique measurement of $E(B-V)$ appears possible beyond this, but we can say that an EW = 2.10 ± 0.22 Å requires a minimum of $E(B-V)_{\mathrm{host}} \gtrsim 0.5$ mag. The Milky Way foreground extinction is also significant along this line of sight, with $E(B-V)_{\mathrm{MW}} = 0.2$ mag (E. F. Schlafly & D. P. Finkbeiner 2011). Throughout the rest of this Letter, we apply a total extinction of $E(B-V)_{\mathrm{total}} = 0.7$ mag, noting that a somewhat higher value cannot be discounted. In Section 3.3.2 we show that fitting the light curves with physical models and allowing the extinction prior to vary recovers a favored value compatible with our adopted value where $R_V = 3.1$.

3.2. Light Curves

The light curves of SN 2023zaw are shown in Figure 1. Shortly after discovery, SN 2023zaw reached a maximum brightness of $r = 17.6$ mag and $g = 18$ mag. Due to the short rise time, we only observe the rising portion of the light curve in the *go* bands. We determine a time of maximum light of MJD 60287.1 ± 0.2 from fitting a polynomial to the ZTF *g* band. The rapid rising phase of the light curve is not well observed, but the time from explosion to *g*-band peak is constrained to be less than 4 days by the ATLAS *o*-band nondetections (at depths corresponding to M_o of −14.5 and −14.8 mag) at 2.7 and 1.8 days prediscovery, respectively. The photometric evolution after maximum light is similarly rapid. SN 2023zaw evolves extremely fast when compared to the representative Type Ib SN 2007Y (M. Stritzinger et al. 2009) in Figure 2. Initially SN 2023zaw fades ∼3 mag in ∼10 days in the *r* band, with SN 2007Y fading by less than a magnitude during the same interval. During this early rapid fade, SN 2023zaw is comparable to SN 2019bkc, the fastest known Type I SN. By around 10 days after maximum, SN 2023zaw settles to an apparent radioactive tail, which we observe in the *riz* bands for approximately 40 rest-frame days.

3.3. Light-curve Modeling

We use the Modular Open Source Fitter for Transients `MOSFiT`,[18] which is a `Python`-based modular code that evaluates a user-defined physical model directly against the multicolor observed light curves of transients. A detailed description of the motivation, usage, and structure of the code can be found in J. Guillochon et al. (2018) and M. Nicholl et al. (2017); V. A. Villar et al. (2017) provide thorough discussion of the modeling framework and simplifying assumptions and explain the magnetar, nickel, and circumstellar material (CSM) interaction models.

---

[18] https://github.com/guillochon/MOSFiT

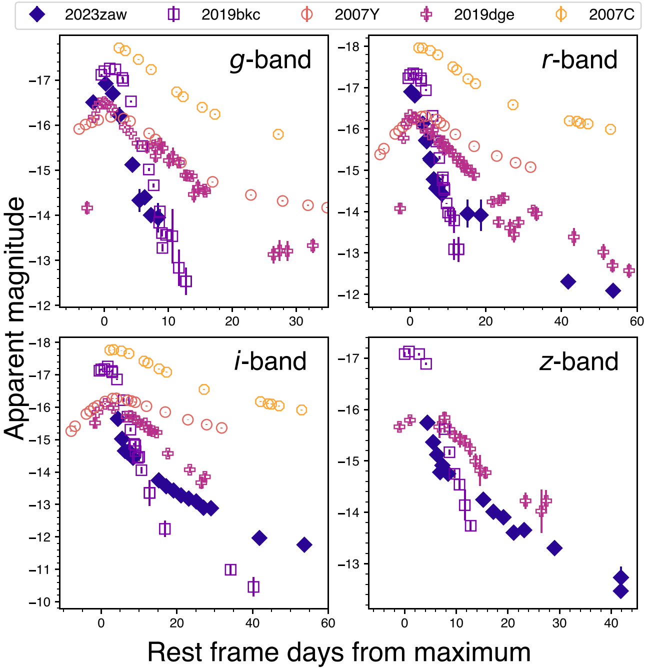

Figure 2. Light curves of SN 2023zaw in the *griz* bands compared to the fast SNe SN 2019bkc (P. Chen et al. 2020; S. J. Prentice et al. 2020) and SN 2019dge (Y. Yao et al. 2020) and the representative Type Ib SNe SN 2007Y (M. Stritzinger et al. 2009) and SN 2007C (M. R. Drout et al. 2011; M. D. Stritzinger et al. 2018). Each light curve is in the rest frame and has been corrected for Milky Way and host galaxy extinctions (M. R. Drout et al. 2011). These SNe were chosen to represent the population of ultrastripped SNe and typical Type Ib SNe.

The code uses semianalytical approximations for a range of luminosity sources (e.g., radioactive decay, magnetar spin-down, CSM interaction). Radiative transfer through the ejecta uses the simplified approach of W. D. Arnett (1982), enabling the model realizations to be evaluated rapidly for Bayesian fitting. The radius of the photosphere is calculated assuming a constant velocity at early times, followed by recession at a constant temperature once the ejecta cool to a critical value (see M. Nicholl et al. 2017 for a full description). Finally, an analytic model SED is calculated and converted to magnitudes using the filter transmission function for evaluation against the input data.

This last step is perhaps the biggest approximation and is worth discussing in some detail. When fitting analytic models to transient data, an assumption has to be made about the SED somewhere in the process. This could be on the data side (estimating the bolometric luminosity from filtered data before fitting) or on the model side (translating a model luminosity into bands of interest using a model SED). In the limit of exquisite multiband data, the former approach is more reliable, as the bolometric luminosity can be well constrained from the data and bolometric models are less subject to the uncertain radiative transfer that controls the emergent SED. However, for many real transients, observations cover only a limited portion of the SED, and not all bands are obtained at all times (e.g., transients are often observed rising in only one or two bands before follow-up is triggered; at late times we often lose sensitivity in the blue bands first as transients cool). In this case, significant SED assumptions must be made on the data side if we want to construct a bolometric light curve (e.g., extrapolating in wavelength with an assumed blackbody SED, or extrapolating in time by assuming a constant temperature at early or late times).

The impact of these choices on subsequent model fits can be very difficult to quantify. For this reason, `MOSFiT` typically fits directly to multiband data, assuming that the model emits an SED that can be described analytically—usually a blackbody with time-variable temperature, calculated from the luminosity using the Stefan–Boltzmann law. Although this represents a major simplification of the true SED, in practice the same SED assumption is used whether we are constructing a bolometric light curve from limited bands or fitting to data in multiple bands. The advantage of the latter approach is that it removes the need to extrapolate in the time dimension, and in principle the model posteriors will reflect the uncertainties in the photospheric temperature. This makes it possible to model a wide range of transients, not only those with excellent multiband data. Fitting in multiband space provides additional color information that can help to constrain extinction, which is important for transients like SN 2023zaw that have uncertain host extinction. A bolometric light-curve analysis can also help in this regard, and to ensure consistency, `MOSFiT` also enables the user to output a bolometric light curve for any given fit, which can be compared to a bolometric light curve estimated from the data. In this study, we will fit to the multiband data but ensure that we check for consistency in this way (see Figure 1).

In this work we use the `dynesty` (J. S. Speagle 2020) nested sampling package in `MOSFiT` to evaluate posteriors for a series of different models. For all models we assume an optical opacity $\kappa = 0.1\,\mathrm{cm^2\,g^{-1}}$ and a gamma-ray opacity $\kappa_\gamma = 0.027\,\mathrm{cm^2\,g^{-1}}$. We apply a constraint to the host galaxy H column density of $n_{\mathrm{H,host}} > 3.4 \times 10^{21}\,\mathrm{cm^{-2}}$ for consistency with our adopted minimum host extinction $E(B-V)_{\mathrm{host}} \gtrsim 0.5$ (Section 3.1), assuming $R_V = 3.1$, using J. A. Cardelli et al. (1989) and the relation $n_{\mathrm{H}}(\mathrm{cm^{-2}})/A_V(\mathrm{mag}) = 2.21 \times 10^{21}$ (T. Güver & F. Özel 2009). All models that are considered in this work are shown in Figure 3, together with the observed light curves of SN 2023zaw. We also show the bolometric light curves of these models compared to the estimated bolometric luminosity of SN 2023zaw in Figure 1. From our models we estimate the values of important parameters (e.g., ejecta mass M_{ej} and nickel fraction f_{Ni}); these parameters are quoted in the text. We reemphasize that our model fits use simplified analytic prescriptions, and as with any models, they include significant systematic errors that are difficult to quantify. Despite this caveat, these analytic models are thought to be reliable at the order-of-magnitude level, and our results are readily comparable to previous applications of `MOSFiT` in the stripped-envelope SN (SESN) literature (M. Nicholl et al. 2017; S. Gomez et al. 2022).

The rising phase of SN 2023zaw is poorly sampled compared to the peak and tail of the light curve, which makes it difficult to achieve a good fit to the early light curve. Following W. D. Arnett (1982) and J. C. Wheeler et al. (2015), we use the observed rise time t_r and an estimate of the photospheric velocity v_{ph} to estimate an ejecta mass M_{ej}. This approach assumes a homologously expanding and spherical ejecta but provides a simple estimate of $M_{\mathrm{ej}} \sim 1/2 \cdot \beta \cdot c/\kappa \cdot v_{\mathrm{ph}} t_r^2$ (J. C. Wheeler et al. 2015) using the photon diffusion timescale. We assume $\beta = 13.7$ (W. D. Arnett 1982), though in reality this depends on the unknown ejecta density profile; c is the speed of light, and κ is the opacity. To approximate the rise time, we adopt the midpoint between the last nondetection and the first

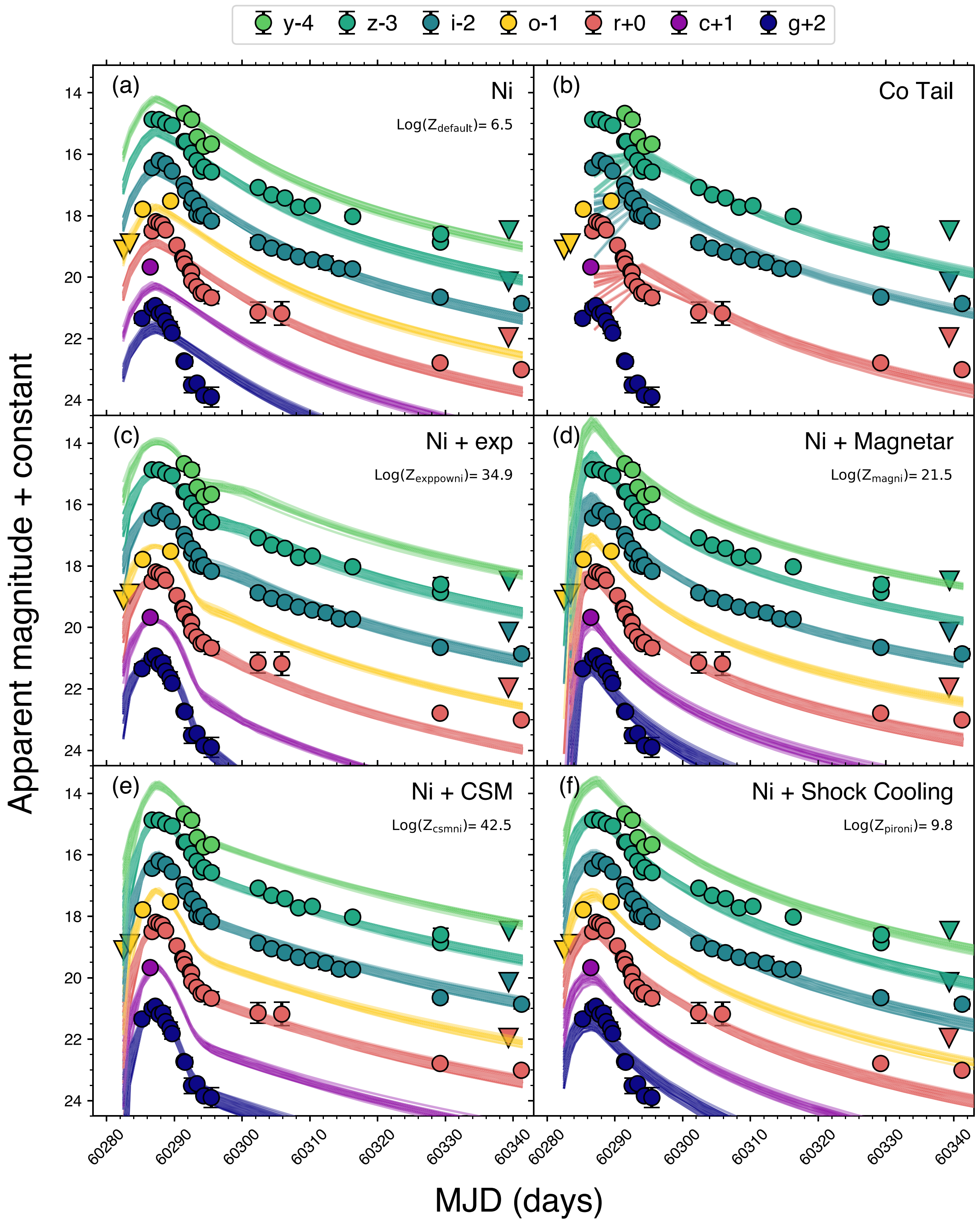

Figure 3. Results of the `MOSFiT` (J. Guillochon et al. 2018) model analysis for each physical model compared to the complete light curves, where downward-pointing arrows are upper limits, realizations are repented as solid lines, and band colors match those in Figure 1. Panel (a) shows nickel-only model realizations. Panels (c), (d), and (e) show the nickel + exp model (J. Guillochon et al. 2018), magnetar + nickel model (M. Nicholl et al. 2017), and circumstellar material interaction + nickel (V. A. Villar et al. 2017) model, respectively. Panel (b) shows a fit to only the late-time light curve to estimate a synthesized nickel mass, and panel (f) shows shock cooling emission + nickel, where the shock cooling treatment follows (A. L. Piro et al. 2021). The Bayesian evidence for each model is calculated for model comparison. When quoting the evidence for each model, the name of each model in the `MOSFiT` code is used to ensure the reproducibility of these results. Model evidence is not included in panel (b), as the model is only evaluated against the light-curve tail.

detection as the explosion epoch (MJD 60284.3, which is ~0.9 days before detection) and the g-band peak for the time of maximum; this gives $t_r \sim 2.75$ days. Using the photospheric velocity $v_{\rm ph}$ derived from spectral modeling in Section 3.4, this analysis estimates an ejected mass $M_{\rm ej} \sim 0.07\, M_\odot$. By allowing a ±1-day uncertainty on the rise time, our mass estimate could vary by up to $0.06\,M_\odot$. To capture this constraint, we adopt a prior on the ejecta mass $M_{\rm ej} = 0.07 \pm 0.06 M_\odot$ for all models.

3.3.1. Nickel Decay

We first attempt to fit the multiband light curves with heating only from ^{56}Ni decay, using the built-in `defaultMOSFiT` model (D. K. Nadyozhin 1994; J. Guillochon et al. 2018). We assume that the ejecta is spherical, with constant gamma-ray and optical capacities, and that the Ni is concentrated in the center of the SN, closely following W. D. Arnett (1982). The details of the `MOSFiT` diffusion implementation are described in M. Nicholl et al. (2017). Here we highlight that $1 - e^{-\psi_{\rm leak} t^{-2}}$ describes the fraction of the input energy that is thermalized, where the leakage parameter is $\psi_{\rm leak} = \frac{3\kappa_\gamma M_{\rm ej}}{4\pi v_{\rm ej}^2}$ (S. Q. Wang et al. 2015), and $\kappa_\gamma = 0.027\,{\rm cm^2\,g^{-1}}$. With this prescription, only a decreasing fraction of the ^{56}Ni decay energy is able to heat the ejecta as time increases.

Despite a reasonable agreement with *i*-band observations, overall this model does not provide a satisfactory fit to the light curves of SN 2023zaw . During the SN rise, the model conflicts with the deep ATLAS *o*-band limits and fails to reproduce the maximum luminosity in the *gcr*bands. The model clearly diverges from the late-time *rz*-band tail and only adequately matches the decline between MJD 60300 and MJD 60320. We find that the most probable model ejects $M_{\rm ej} \simeq 0.06\,M_\odot$ of material with a large ^{56}Ni fraction $f_{\rm Ni} \simeq 0.90$ and a reasonable SN-like ejecta velocity $v_{\rm ej} \simeq 6400\,{\rm km\,s^{-1}}$. This implies that $M_{\rm Ni} \simeq 0.05\,M_\odot$ was synthesized in the explosion; this is lower than typical for Type Ib SNe (J. P. Anderson 2019; Ó. Rodríguez et al. 2023). More problematic is the very large nickel fraction, contradicting our observed spectra. An ejecta of mostly ^{56}Ni and its decay products should be dominated by iron-group absorption in the blue; this is not observed in the spectra of SN 2023zaw. Additionally, a nickel yield of $M_{\rm Ni} \simeq 0.05\,M_\odot$ is difficult to rationalize in the context of the ultrastripped SNe (see, e.g., discussion from R. Sawada et al. 2022 on iPTF14gqr). The light-curve tail begins approximately 10 days after maximum. The decline rate slows and follows a power-law decline, an evolution that is similar to the *i*-band tail of the fast-fading SN 2019bkc (P. Chen et al. 2020; S. J. Prentice et al. 2020), where this was attributed to radioactivity. Clearly, a ^{56}Ni-only model does not reproduce our observations, requires an unrealistic nickel fraction, and can only adequately explain the light-curve tail. Therefore, we exclude the scenario where nickel decay is the only mechanism powering the light-curve peak of SN 2023zaw and seek an explanation with another mechanism in addition to nickel decay.

Assuming that the heating at *late times* is powered only by decay of ^{56}Co to ^{56}Fe, we can estimate a synthesized nickel mass for SN 2023zaw. We apply the same model as before but with a restriction to fit only the late-time *riz*-band data (MJD > 60300). The model likelihood is only evaluated against the late-time photometry, but we provide a prior constraining the explosion epoch between the last ATLAS nondetection (MJD 60282.51) and the first detection (MJD = 60285.23). The tail-only fit requires that $M_{\rm Ni} \simeq 0.006\,M_\odot$ was synthesized and ejected to power this phase of the light curve. Seeking to verify our method, we also reanalyze the light-curve tail in SN 2019bkc and find a nickel mass $M_{\rm Ni} \simeq 0.005\,M_\odot$, which is compatible with the $M_{\rm Ni} = 0.001{-}0.01\,M_\odot$ estimated by P. Chen et al. (2020). We also perform a consistency check by fitting the late-time bolometric tail using the method of B. Katz et al. (2013) and N. Wygoda et al. (2019), finding a consistent nickel mass of $M_{\rm Ni} = 0.002{-}0.006\,M_\odot$.

Motivated by the poor agreement of the nickel decay model to the initial light curve but apparent agreement with the light-curve tail, we consider a generalized early-time heating source plus a nickel decay tail. This approach aims to investigate the compatibility of the observed light curves with a nickel power source and an additional mechanism without placing assumptions on the exact nature of the additional source. Using `MOSFiT`, we adopt a physics-agnostic analytical prescription for an exponentially rising additional energy source that declines from its maximum ($t_{\rm peak}$) following a power law (named `exppow`). It is described by $L = L_{\rm scale} \cdot (1 - e^{-t/t_{\rm peak}})^{\alpha} \cdot (t/t_{\rm peak})^{-\beta}$, where $L_{\rm scale}$, α, β, and $t_{\rm peak}$ are free parameters. Combining the `default` and `exppow` models, we created a new `MOSFiT` model called `exppowni`.

We fit the `exppowni` model as before using the same constraints on opacity and host galaxy extinction. The model realizations are shown in Figure 3. We see good agreement with observations and consistency with the ATLAS nondetections, the observed color, and late-time luminosities. We estimate a nickel mass of $M_{\rm Ni} \simeq 0.006\,M_\odot$, which is in agreement with the fit for only the light-curve tail. It is clear that an additional luminosity source is required to simultaneously match the fast rise, the peak luminosity, and the observed ^{56}Co tail. The parameterized nature of the `exppowni` model provides insight into the timescale and energetics of the additional luminosity source. The nonradioactive heating reaches $t_{\rm peak}$ between 1.6 and 2.6 days after explosion and dominates the luminosity during this phase with a scale luminosity $L_{\rm scale} \sim 10^{42}\,{\rm erg\,s^{-1}}$.

3.3.2. Circumstellar Material Interaction + Nickel

We next investigate interaction with nearby CSM as the possible extra energy source for SN 2023zaw. CSM interaction can produce unusual and rapidly evolving transients (e.g., T. Moore et al. 2023; H. Kuncarayakti et al. 2023; T. Nagao et al. 2023; D. A. Perley et al. 2022). We use the `CSMNI` model in `MOSFiT` (V. A. Villar et al. 2017; B. Jiang et al. 2020; T. Moore et al. 2023), which combines the luminosity of ^{56}Ni decay and heating from shock propagation following an ejecta–CSM collision. The CSM interaction physics is implemented following the treatment of E. Chatzopoulos et al. (2013). We use the adapted model setup used by T. Moore et al. (2023) and S. Srivastav et al. (2023), where the onset of interaction is delayed until the ejected material reaches an inner CSM radius.

We evaluate the `csmni` model against our observations and show the CSM model realizations in Figure 3. This model fits the light-curve peak very well and matches the overall light-curve evolution in all bands, including close agreement with the late-time tail. When compared to the pseudobolometric light curve, we achieve excellent agreement with the observed data. The derived model parameters are $M_{\rm ej} \simeq 0.069\,M_\odot$, $f_{\rm Ni} \simeq 0.13$, $r_{\rm csm} \simeq 63$ au, and $M_{\rm csm} \simeq 0.23\,M_\odot$, where $M_{\rm csm}$ is the mass of the CSM material and $r_{\rm csm}$ is the CSM radius. The CSM mass and radius show strong degeneracy. The derived kinetic energy for this model is low at $E_k \sim 10^{49}$ erg. This model implies $M_{\rm Ni} \simeq 0.008\,M_\odot$, which is compatible with our estimate from fitting only the light-curve tail.

The CSM interaction treatment assumes that the progenitor star is embedded in a spherically symmetric CSM shell with a power-law density profile described by a single power-law index s, where $s = 2$ is a wind-like CSM and $s = 0$ is a shell of constant density; see V. A. Villar et al. (2017) for a full model description. Treating it as a free parameter in our fit, we find $s \simeq 0.68$, which does not indicate a strong preference for a constant-density shell or wind mass-loss history.

We note that the +61-day spectrum of SN 2023zaw (K. K. Das et al. 2024) shows narrow helium lines, which are also consistent with circumstellar interaction. These results suggest significant late-stage mass loss consistent with the binary mass transfer scenario simulated for a Type Ib/c SN progenitor in S. C. Wu & J. Fuller (2022). We note that if we allow the prior on the extinction of the host galaxy to broadly vary, the model converges to a host $E(B-V) \simeq 0.6$ ($R_V = 3.1$), which is similar to our adopted extinction estimate from Section 3.1.

3.3.3. Central Engine + Nickel

As an alternative, we next investigate the feasibility of central engine heating as the additional energy source using the magnetar central engine + nickel (`magni`) model described by M. Nicholl et al. (2017) and S. Gomez et al. (2022). This combines the luminosity of magnetar spin-down (D. Kasen & L. Bildsten 2010; S. E. Woosley 2010) with radioactive heating. This model reproduces the data significantly better than radioactive heating alone, as shown in Figure 3, and matches the peak but diverges from the *riz*-band tail. This model achieves agreement within the uncertainties to the pseudobolometric light curve in Figure 1. Our derived `magni` model parameters are ejecta mass $M_{\rm ej} \simeq 0.055\,M_\odot$, nickel fraction $f_{\rm Ni} \simeq 0.08$, and $M_{\rm Ni} \simeq 0.004\,M_\odot$. We find central engine parameters of $P_{\rm spin} \simeq 6.3$ ms and $B_\perp \simeq 0.19 \times 10^{14}$ G. The *B*-field required from our models is consistent with the population of superluminous SNe. However, the spin period, $P_{\rm spin}$, is toward the longer end of the range of 1–6 ms (e.g., K. Kashiyama et al. 2016; M. Nicholl et al. 2017). Given the low ejecta mass, the region of the ejected material that is being heated by the central engine should be visible. Therefore, unless the oxygen is doubly ionized, we would expect the W-shaped O II absorption lines to be present in the spectrum, which are the characteristic signature of central engines in Type I superluminous SNe (P. A. Mazzali et al. 2016; R. M. Quimby et al. 2018); unfortunately, this region of the SN 2023zaw spectrum was not observed. Allowing the extinction of the host galaxy to broadly vary, the model converges to a host $E(B-V) \simeq 0.6$; this is similar to the value returned by the `csmni` model and our adopted extinction estimate.

3.3.4. Shock Cooling + Nickel

Finally, we consider the combination of ^{56}Ni and shock cooling emission following the analytical model from A. L. Piro et al. (2021). In this scenario the progenitor star possesses an extended envelope into which energy is deposited by the SN blast wave; the envelope then radiates this energy as it cools. We have added this model to `MOSFiT` as the `pironi` model. We show our model realizations in Figure 3. Our model requires $f_{\rm Ni} \simeq 0.01$, $M_{\rm ej} \simeq 0.04\,M_\odot$, $M_{\rm env} \simeq 0.3\,M_\odot$, and $R_{\rm star} \simeq 10^{10.5}$ cm. However, the shock cooling model shows relatively poor agreement with the overall light curve of SN 2023zaw. It contradicts the early ATLAS nondetections and does not reproduce the observed tail, where the model is underluminous.

We note that this model has better agreement with observations if we instead adopt the host galaxy extinction estimate from K. K. Das et al. (2024), $A_{v,\rm host} = 1.12$ mag, $E(B-V) = 0.36$ ($R_V = 3.1$). Evaluating the `pironi` model with this value of host extinction, we find overall similar parameter values: $f_{\rm Ni} \sim 0.009$, an envelope mass $M_{\rm env} \sim 0.3\,M_\odot$, an ejected mass $M_{\rm ej} \sim 0.03\,M_\odot$, and a stellar radius $R_{\rm star} \sim 10^{10.3}$ cm.

3.3.5. Model Comparison

To compare the models, we use the Bayesian model evidence (marginal likelihood) scores for each model. These are returned by `MOSFiT` when using the nested sampler `Dynesty` (J. S. Speagle 2020). All `MOSFiT` analysis in this work uses a nested sampling approach to enable comparison between models. From the Bayesian evidence scores, a Bayes factor (BF) can be used to compare two models. The BF comparing model x and model y is given by $B \equiv Z_x/Z_y$, where Z_i is the Bayesian evidence for model i. A BF $B > 10$ indicates a strong preference, and $B > 100$ is considered definitive.

We find a BF $Z_{\rm expowni}/Z_{\rm nickel} \sim 10^{21}$, where $Z_{\rm exppowni}$ and $Z_{\rm nickel}$ are the evidence for their respective models; this shows evidence favoring an additional powering source. This statistical test and the poor agreement of the pure ^{56}Ni model with the light curve provide evidence that SN 2023zaw requires an additional power source. Comparing our Ni model and shock cooling model, we find $Z_{\rm pironi}/Z_{\rm nickel} \sim 10^1$; the shock cooling + Ni model is preferred over Ni alone. Comparing between models in this way, our analysis favors the CSM + Ni model above all others. When comparing the alternative models, we calculate $Z_{\rm csmni}/Z_{\rm magni} \sim 10^{10}$, favoring CSM interaction over the spin-down of a newly born neutron star. However, we note that the `MOSFiTCSMNI` model is the most complex model evaluated in this work and the most flexible, while likely oversimplifying the physics involved. While the CSM + Ni model reproduces the light-curve tail luminosity better than any other model, we also note that the blackbody spectrum assumed in `MOSFiT` may be unreliable at this phase, as the ejected material becomes transparent.

Through `MOSFiT` modeling we have shown that the total emission of SN 2023zaw cannot be explained with radioactivity alone, as the required $f_{\rm Ni} \simeq 0.9$ is incompatible with the spectroscopic observations (discussed in Section 3.4). We have found evidence that suggests that another energy source is required that peaks early in the evolution of SN 2023zaw and dominates the emission at this phase. We disfavor shock cooling emission as this additional source owing to poor agreement with the multicolor photometry, in particular our ATLAS nondetections and failure to reproduce the pseudobolometric light curve. Our analysis favors CSM interaction + nickel, with a CSM mass that is large but not beyond theoretical predictions (S. C. Wu & J. Fuller 2022), but cannot rule out a central engine + nickel model for SN 2023zaw. We consider both models as viable explanations for SN 2023zaw.

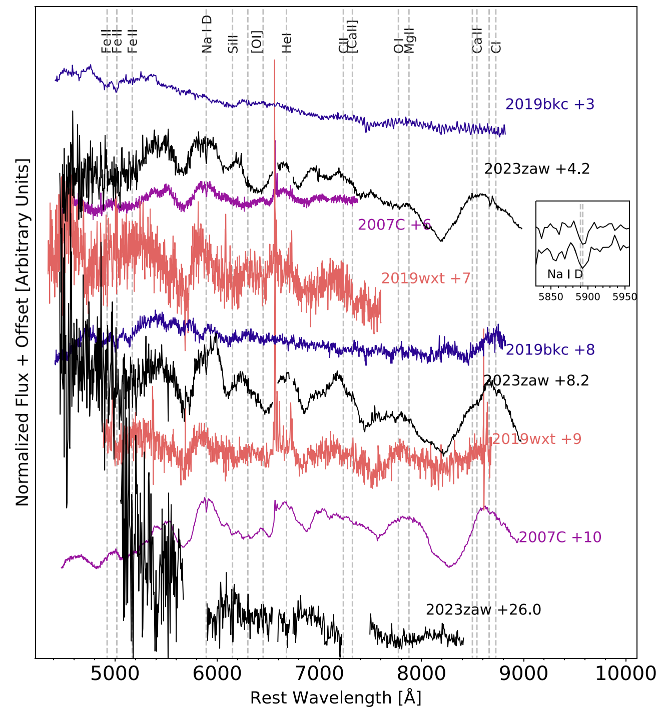

Figure 4. Optical spectroscopy of SN 2023zaw. The phase in days relative to maximum light is indicated. These spectra have been telluric and Galactic line-of-sight extinction corrected and corrected for host galaxy recessional velocity. The inset shows the blended Na I D lines in the +4.2- and +8.2-day spectra. We also include spectra from SN 2019wxt (I. Agudo et al. 2023), SN 2007C (M. Modjaz et al. 2014), and SN 2019bkc (P. Chen et al. 2020; S. J. Prentice et al. 2020) and include the approximate phase of each observation.

3.4. Spectral Modeling and Analysis

We present post-peak spectra taken +4.2, +8.2, and +26.0 days after maximum light in Figure 4. Our first spectrum (taken at +4.2 days) shows well-developed absorption features and a prominent Ca II near-IR triplet. Weak Fe II features may exist around 4500–5000 Å, and we find that a 5700 K blackbody produces a continuum in agreement with the observed spectrum. As noted in Section 3.1, the spectra show a prominent Na I D line blend.

The spectra show little evolution between the +4.2- and +8.2-day observations, considering the rapidly evolving light curve. At +8.2 days, the spectroscopic features have more developed line profiles and a broad emission feature at 7100 Å is apparent. Our final observation at +26.0 days is mostly featureless and likely dominated by the host galaxy; therefore, we exclude it from further quantitative analysis.

SN 2023zaw has been proposed as a ".Ia" SN and compared to the .Ia SN candidate SN 2010X (V. Karambelkar et al. 2023b). The .Ia SNe are the theorized explosion of a helium shell on the surface of a white dwarf (K. J. Shen & L. Bildsten 2009; K. J. Shen et al. 2010). In Figure 5 we present a spectroscopic comparison to He shell detonation models (S. A. Sim et al. 2012). Although the model provides some agreement with the SED of the observed spectrum at +4.2 days, it predicts emission at ∼5700 Å, where in the observed spectrum we instead see strong He I absorption. At +8.2 days, the differences between the model and our observation become starker, with the He detonation model showing strong emission features not present in the data. With such clear divergence from the He detonation model, we rule out a .Ia origin for SN 2023zaw, in agreement with K. K. Das et al. (2024).

As shown in Figure 4, SN 2023zaw exhibits a striking similarity to SN 2019wxt, in terms of both the observed lines and the overall SED shape. Here we undertake a similar process to that presented by I. Agudo et al. (2023), using TARDIS to model the photospheric-phase spectra. TARDIS (W. E. Kerzendorf & S. A. Sim 2014) is a one-dimensional, time-independent, Monte Carlo radiative transfer spectral synthesis code capable of simulating the spectra of an array of different explosive transients. Here we briefly describe the code, but for full details of our implementation see W. E. Kerzendorf & S. A. Sim (2014) and I. Agudo et al. (2023). In brief, TARDIS simulates the propagation of *radiation packets* (analogous to photons) through some model ejecta structure, as defined by user inputs. These packets undergo free e^- scattering and bound–bound interactions with the ejecta material, and the ones that emerge from the simulation are used to compute a synthetic spectrum, which is compared to observations (usually through a visual "χ-by-eye" approach; see, e.g., M. Stehle et al. 2005). We then iteratively vary our input parameters to improve agreement between model and observation, until satisfactory agreement with the data has been reached.

While TARDIS is a time-independent code, one can evolve the input parameters to obtain a sequence of self-consistent models, as we do here for the +4.2- and +8.2-day spectra of SN 2023zaw. These user-defined input parameters include specifying the time since explosion, $t_{\rm exp}$ (which we set to be 2 days premaximum), the inner and outer boundary of the computational domain (defined in velocity space, where $v_{\rm inner}^{+4.2\,\rm d} = 12,500\ \rm km\ s^{-1}$, $v_{\rm inner}^{+8.2\,\rm d} = 5000\ \rm km\ s^{-1}$, and $v_{\rm outer} = 20{,}000\ \rm km\ s^{-1}$), and the abundance and density of the ejecta material (here we use a uniform abundance across the entire ejecta and across both epochs; see Table 1), and we invoke an exponential profile, where

$$\rho(v, t_{\rm exp}) = 2 \times 10^{-12} \times \exp\left[\frac{-v}{6000\ \rm km\ s^{-1}}\right] \times \left(\frac{2\ \rm days}{t_{\rm exp}}\right)^3\ \rm g\ cm^{-3}. \tag{1}$$

We use the `dilute-lte`, `nebular`, and `scatter` approximations for excitation, ionization, and line treatment, respectively, as well as including the `recomb-nlte` He treatment (as presented by A. Boyle et al. 2017), to capture non-LTE (NLTE) excitation effects for He I. Our approximately LTE ionization and excitation treatments for all other ions are well motivated, as the phases we are probing are within the photospheric regime.

We present our model fits in Figure 5. The observations possess a number of prominent absorption features, located at ∼5700, 6100, 6400, 6800, 7400, and 8200 Å. We find that we can reproduce the +4.2-day spectrum with a relatively simple composition, made up of He, O, Si, and Ca, where the 6100 Å feature is produced by Si II, the 7400 Å feature is produced by O I, the 8200 Å feature is produced by Ca II, and all others (i.e., 5700, 6400, and 6800 Å) are produced by He I. We overproduce the 5700 Å He absorption feature, and we do not reproduce the continuum blueward of $\lesssim$5400 Å, but overall the fit to the data is good.

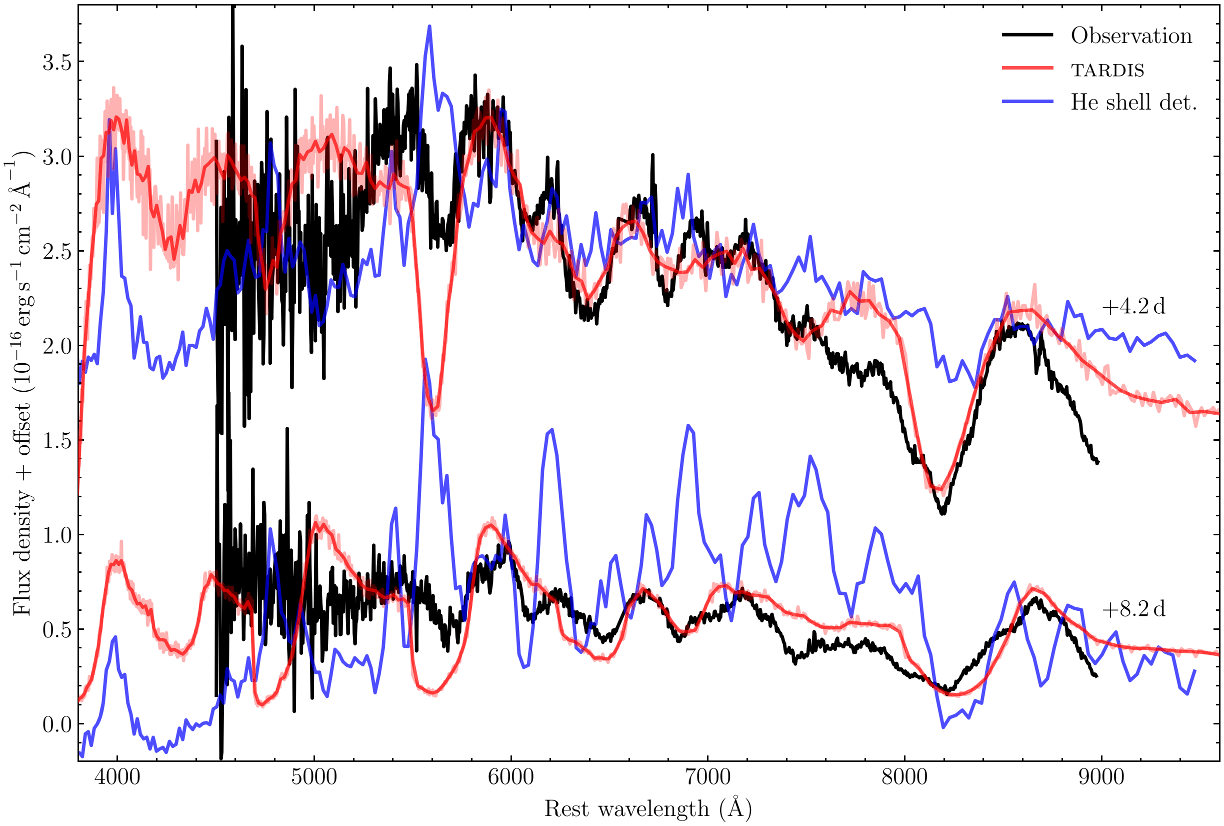

Figure 5. Best-fitting TARDIS models (red), compared to the +4.2- and +8.2-day observed spectra of SN 2023zaw (black). The +4.2-day observed spectrum and associated model spectra have been vertically offset for clarity (by 6×10^{-17}erg s^{-1} cm^{-2} Å^{-1}). Also plotted are two model spectra from a helium shell detonation simulation (blue) presented by S. A. Sim et al. (2012). These models have phases comparable to those of the observed spectra ($\Delta t < 0.13$ days) and have been rescaled and arbitrarily offset to roughly match the continua of the observed spectra.

Table 1
TARDIS Model Compositions

Element	Mass Fraction
He	0.50
O	0.30
Si	0.20
Ca	5×10^{-6}

We note that the NLTE He treatment within TARDIS is a simple, empirically derived approximation designed to account for the effects of recombination from He II → He I. As such, it is possible that the estimated level populations within our TARDIS simulation have deviated from the true level populations. This possible issue has been noted before and was proposed as the reason behind the disagreement between the relative strengths of He features in the case of SN 2019wxt (I. Agudo et al. 2023). There, they manually altered the relative level populations of He I to better match the observed relative strengths of the He I features. Here we opt to not explore such variations, as our focus is on constraining the elements that dominate the composition in the line-forming region of the ejecta material of SN 2023zaw.

Attempts to fit the observations in a more detailed manner than presented here should be approached with caution, given that we have no reliable constraint on the true level of extinction. As a result, the true continuum of these observed spectra could be much bluer than what we present here (see Section 3.1 for details on our extinction estimates), which would significantly alter the agreement of our models to the data.

Although our model composition is quite rudimentary, it aligns with our SN Ib classification, and not SN .Ia. We are able to constrain the composition to be ∼80% He and O and ∼20% Si (in the line-forming region). Our inner velocity estimates derived from this modeling ($v_{\rm inner}^{+4.2\,\rm d} = 12,500$ km s^{-1} and $v_{\rm inner}^{+8.2\,\rm d} = 5000$ km s^{-1}) indicate that the photosphere is receding quickly into the ejecta material, consistent with a small mass of ejected material.

3.5. Volumetric Rates

Here we present a preliminary volumetric rate estimate for SN 2023zaw–like rapidly evolving SESNe. We use the methodology described by S. Srivastav et al. (2022) for estimating rates of SNe Iax. We consider rapidly evolving SESNe detected by the ATLAS survey that occurred within a distance of 100 Mpc during a 5 yr window spanning from 2017 September 21 to 2022 September 20 (S. Srivastav et al. 2022). To estimate the recovery efficiency of SN 2023zaw–like transients within 100 Mpc, we use the ATLAS survey simulator (O. McBrien 2021). We use Gaussian-process-interpolated ATLAS *c*- and *o*-band light curves of SN 2023zaw, produced by interpolating the light curves using the public `extrabol` (I. Thornton et al. 2023) code. These were then injected 10,000 times at a range of times, sky locations, and redshift bins spanning up to $D = 100$ Mpc in the simulation. A simulated transient was considered to be recovered as a detection if it produced a minimum of six to eight detections of 5σ (or greater) significance. Although difference detections in the ATLAS data stream are flagged as candidate transients if they produce three individual 5σ detections on any given night, this criterion is more realistic since human scanners will be confident about promoting candidates to the TNS if they have detections over at least two distinct nights.

The volumetric rate is thus estimated using

$$R = \frac{N}{\eta V T}, \tag{2}$$

where T is the time duration of the mock survey, N is the number of ultrastripped SNe detected within the considered time duration, η represents the recovery efficiency from the ATLAS survey simulator, and V is the volume probed within 100 Mpc. We consider $N = 3$, representing SN 2019bkc (P. Chen et al. 2020; S. J. Prentice et al. 2020), SN 2019dge (Y. Yao et al. 2020), and SN 2021agco (S. Yan et al. 2023). The recovery efficiency obtained from the survey simulator is $\eta \approx 0.06 \pm 0.02$.

From the above, we estimate a rate of $R \approx 2.5^{+2.5}_{-1.4} \pm 0.9 \times 10^{-6}$ Mpc^{-3} yr^{-1} h_{70}^{3} for rapidly evolving SN 2023zaw–like SESNe, where $h_{70} = H_0/70$. The statistical uncertainty derives from 1σ Gaussian errors from single-sided upper and lower limits for Poisson statistics (N. Gehrels 1986), and the systematic uncertainty is based on the error on the recovery efficiency η. The above rate estimate for SN 2023zaw–like SESNe accounts for ~1%–6% of the CCSN rates and ~5%–20% of the SESN rates computed by C. Frohmaier et al. (2021). We note here that ~15% of transients in the 100 Mpc ATLAS sample do not have a spectroscopic classification (S. Srivastav et al. 2022), and it is possible that the representation of SN 2023zaw–like rapidly evolving SESNe is disproportionately higher within the unclassified sample. Nonetheless, at a few percent of the CCSN rate, these transients clearly constitute a rare class of stellar explosions.

3.6. *Potential Evolutionary Route*

Using the parameters derived from our analysis, we search for potential progenitor systems in the Binary Population and Spectral Synthesis data release (BPASSv2.2.2; J. J. Eldridge et al. 2017; E. R. Stanway & J. J. Eldridge 2018; H. Stevance et al. 2020). Assuming a solar metallicity ($Z = 0.02$), we consider models with $M_{\rm H} < 0.01\,M_\odot$ and hydrogen mass fraction $X < 0.001$ (L. Dessart et al. 2012). We use the inferred low ejecta mass from Section 3.3 of $M_{\rm ej} < 0.1\,M_\odot$ and a low kinetic energy of 10^{50} erg. Additionally, we apply a condition for explodability, commonly a mass threshold of the oxygen–neon core ($>1.38\,M_\odot$), used to determine whether a model is a candidate for core collapse. No models in BPASSv2.2.2 are found to match all of our conditions; however, slightly relaxing the condition to an ONe core mass $>1.30\,M_\odot$ (one significant figure), we find 10 models that fit our criteria. When we include weights dependent on the initial mass function (P. Kroupa 2001), as well as the binary fractions and period distributions (M. Moe & R. Di Stefano 2017), this corresponds to 28 systems per million solar masses.

Grids of stellar evolution models such as BPASSv2.2.2 do not contain all possible observable outcomes; however, we find candidate progenitor stars just at the threshold of explodability, motivating the observed rarity of SN 2023zaw–like explosions. The progenitor of SN 2023zaw is very likely a lower-mass star, and the initial masses of our six systems on the cusp of explodability range from 7.5 to 9 $M_\odot$, which are some of the most common massive stars in the Universe. The low rate of SN 2023zaw–like SNe and BPASS results are reconciled if potential progenitors of these SNe fail to explode most of the time, as their cores do not reach the necessary physical conditions. The 10 models with ONe core mass $>1.3\,M_\odot$ represent only 2.6% of the massive stars ($M_{\rm ZAMS} > 7.5\,M_\odot$) that fit our stripping and ejecta mass criteria, and it is unlikely that all of these would explode. This is in agreement with the calculated rates in Section 3.5 of a few percent of the CCSN rate.

4. Summary and Conclusions

In this section we summarize the properties of SN 2023zaw.

1. SN 2023zaw shows a rapid rise (<4 rest-frame days) and an initial decline from maximum light, which settles to a radioactive tail 10 days after peak. Comparisons to ultrastripped SNe and rapidly evolving SNe show that SN 2023zaw is comparable to SN 2019bkc (P. Chen et al. 2020; S. J. Prentice et al. 2020). We consider radioactive nickel as the power source for SN 2023zaw , finding that nickel alone cannot power both the peak and the tail of the light curve, unlike SN 2019dge and SN 2019wxt (Y. Yao et al. 2020; I. Agudo et al. 2023). An additional power source is required.
2. We consider several additional powering mechanisms and use agreement with the pseudobolometric light curve (Figure 1) and multiband photometry (Figure 3) to select a preferred model. This analysis favors interaction with CSM material ($M_{\rm csm} \simeq 0.2\,M_\odot$, $r_{\rm csm} \simeq 63$ au), or powering from a central engine ($P_{\rm spin} \simeq 6$ ms and $B_\perp \simeq 0.2 \times 10^{14}$ G), to boost the initial luminosity before SN 2023zaw settles to a ^{56}Co tail. We note that signatures of interaction were not observed in the spectra, and we suggest that any CSM envelope was swept up by the photosphere before our first spectroscopic observation, with the spectroscopic narrow helium lines only becoming visible at late times.
3. Through spectroscopic comparison we show that SN 2023zaw is similar to Type Ib SNe and shows lines and line strengths similar to SN 2007C (M. Modjaz et al. 2014) and SN 2019wxt (I. Agudo et al. 2023). Monte Carlo radiative transfer modeling with TARDIS shows that SN 2023zaw has a composition dominated by He, O, and Si. The spectroscopic evolution is not compatible with He shell detonation models.
4. A simulated ATLAS survey and estimate of the spectroscopic completeness of the ATLAS Volume Limited Survey ($D < 100$ Mpc) yield a rate estimate of $R \approx 2.5^{+2.5}_{-1.4} \pm 0.9 \times 10^{-6}$ Mpc^{-3} yr^{-1} h_{70}^{3}. SN 2023zaw–like transients could be as common as ~1%–6% of the CCSN rate. Searching for potential progenitor stars in BPASS models, we propose that SN 2023zaw–like events are the result of lower-mass progenitors ($M_{\rm ZAMS} = 7.5–9\,M_\odot$) whose cores are at the threshold of explodability. The low observed rate of these SNe is then a result

of the fact that only a few percent of these stars end with a core mass sufficient to result in core collapse.

We have shown SN 2023zaw to be part of a small group of rapidly evolving SNe with a low ejecta mass ($M \simeq 0.07\,M_{\odot}$) and estimated a total nickel mass synthesized in the explosion ($M_{\rm Ni} \simeq 0.006\,M_{\odot}$). Furthermore, we find evidence in favor of an extra luminosity source in addition to the radioactive decay of ^{56}Ni. With our estimate of host galaxy extinction and significant Milky Way extinction in the line of sight, we cannot reproduce the observe light curve with shock cooling emission, as favored by K. K. Das et al. (2024), and instead we favor interaction with a detached CSM, or central engine energy injection, to boost the luminosity of SN 2023zaw.

Acknowledgments

We thank the referee for suggestions and comments that led to an improved manuscript. S.J.S., S.S., K.WS., and D.R.Y. acknowledge funding from STFC grants ST/Y001605/1, ST/X001253/1, ST/X006506/1, and ST/T000198/1. S.J.S. acknowledges a Royal Society Research Professorship. M.N. is supported by the European Research Council (ERC) under the European Union's Horizon 2020 research and innovation program (grant agreement No. 948381) and by UK Space Agency grant No. ST/Y000692/1. T.-W.C. acknowledges the Yushan Young Fellow Program by the Ministry of Education, Taiwan for the financial support. S.Y. acknowledges the funding from the National Natural Science Foundation of China under grant No. 12303046. H.F.S. is supported by the Eric and Wendy Schmidt A.I. in Science Fellowship. Pan-STARRS is primarily funded to search for near-Earth asteroids through NASA grants NNX08AR22G and NNX14AM74G. The Pan-STARRS science products for transient follow-up are made possible through the contributions of the University of Hawaii Institute for Astronomy and Queen's University Belfast. ATLAS is primarily funded through NASA grants NN12AR55G, 80NSSC18K0284, and 80NSSC18K1575. The ATLAS science products are provided by the University of Hawaii, Queen's University Belfast, STScI, SAAO, and Millennium Institute of Astrophysics in Chile. We thank Lulin staff H.-Y. Hsiao, W.-J. Hou, C.-S. Lin, H.-C. Lin, and J.-K. Guo for observations and data management. Based on observations obtained at the international Gemini Observatory (under program ID GN-2023B-Q-125), a program of NSF NOIRLab, which is managed by the Association of Universities for Research in Astronomy (AURA) under a cooperative agreement with the US National Science Foundation on behalf of the Gemini Observatory partnership: the US National Science Foundation (United States), National Research Council (Canada), Agencia Nacional de Investigación y Desarrollo (Chile), Ministerio de Ciencia, Tecnologìa e Innovación (Argentina), Ministério da Ciência, Tecnologia, Inovações e Comunicações (Brazil), and Korea Astronomy and Space Science Institute (Republic of Korea). This work was enabled by observations made from the Gemini North telescope, located within the Maunakea Science Reserve and adjacent to the summit of Maunakea. We are grateful for the privilege of observing the Universe from a place that is unique in both its astronomical quality and its cultural significance. Lasair is supported by the UKRI Science and Technology Facilities Council and is a collaboration between the University of Edinburgh (grant ST/N002512/1) and QUB (grant ST/N002520/1) within the LSST:UK Science Consortium. ZTF is supported by National Science Foundation grant AST-1440341 and a collaboration including Caltech, IPAC, the Weizmann Institute for Science, the Oskar Klein Center at Stockholm University, the University of Maryland, the University of Washington, Deutsches Elektronen-Synchrotron and Humboldt University, Los Alamos National Laboratories, the TANGO Consortium of Taiwan, the University of Wisconsin–Milwaukee, and Lawrence Berkeley National Laboratories.

Facilities: Gemini:Gillett, Swift, PS1, PO:1.2 m, Liverpool:2m.

Software: Astropy (Astropy Collaboration et al. 2013, 2018, 2022), Numpy (C. R. Harris 2020), Matplotlib (J. D. Hunter 2007), Mosfit (J. Guillochon et al. 2018), Hoki (H. Stevance et al. 2020), PSF (M. Nicholl et al. 2023), DRAGONS (K. Labrie et al. 2023a, 2023b)

Appendix
MOSFiT Model Posterior

The MOSFiT model posterior for the `CSMNI` model is presented in Figure 6.

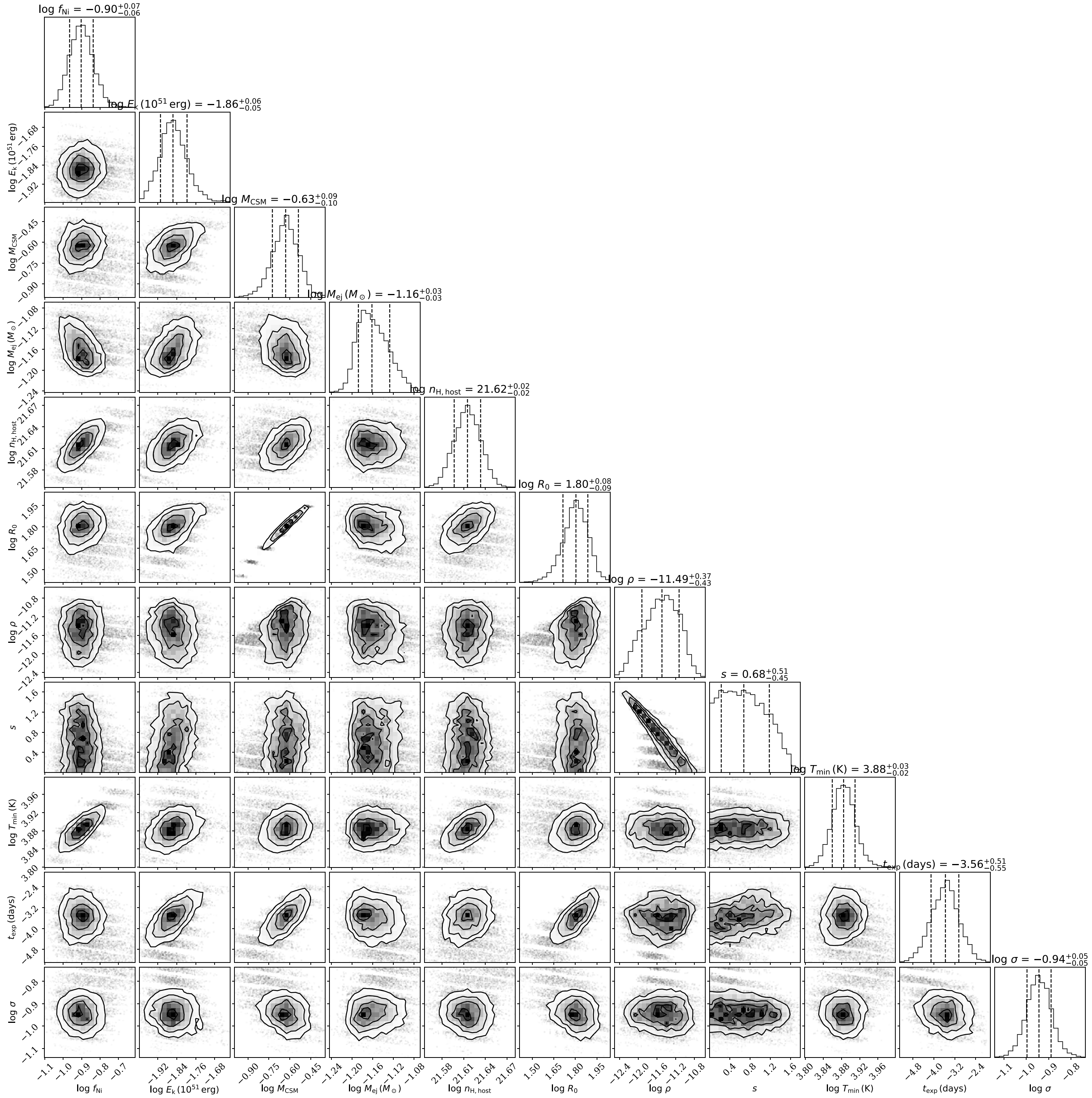

Figure 6. Physical parameter posterior distribution of the circumstellar material + nickel model. The important physical parameters are nickel fraction ($f_{\rm Ni}$), kinetic energy (E_k), CSM mass ($M_{\rm csm}$), ejecta mass ($M_{\rm ej}$), CSM radius (R_0) in units of AU, CSM density (ρ), and $t_{\rm exp}$ relative to the first photometric detection (MJD 60285.23) of SN 2023zaw.

ORCID iDs

T. Moore https://orcid.org/0000-0001-8385-3727
J. H. Gillanders https://orcid.org/0000-0002-8094-6108
M. Nicholl https://orcid.org/0000-0002-2555-3192
M. E. Huber https://orcid.org/0000-0003-1059-9603
S. J. Smartt https://orcid.org/0000-0002-8229-1731
S. Srivastav https://orcid.org/0000-0003-4524-6883
T.-W. Chen https://orcid.org/0000-0002-1066-6098
K. C. Chambers https://orcid.org/0000-0001-6965-7789
J. P. Anderson https://orcid.org/0000-0003-0227-3451
M. D. Fulton https://orcid.org/0000-0003-1916-0664
S. R. Oates https://orcid.org/0000-0001-9309-7873
G. Pignata https://orcid.org/0000-0003-0006-0188
N. Erasmus https://orcid.org/0000-0002-9986-3898
H. Gao https://orcid.org/0000-0003-1015-5367
E. A. Magnier https://orcid.org/0000-0002-7965-2815
P. Minguez https://orcid.org/0009-0003-8803-8643
C.-C. Ngeow https://orcid.org/0000-0001-8771-7554
X. Sheng https://orcid.org/0000-0002-6527-1368
S. A. Sim https://orcid.org/0000-0002-9774-1192

D. R. Young https://orcid.org/0000-0002-1229-2499
K.-J. Zeng https://orcid.org/0009-0001-2319-9169

References

Agudo, I., Amati, L., An, T., et al. 2023, A&A, 675, A201
Anderson, J. P. 2019, A&A, 628, A7
Arnett, W. D. 1982, ApJ, 253, 785
Astropy Collaboration, Price-Whelan, A. M., Lim, P. L., et al. 2022, ApJ, 935, 167
Astropy Collaboration, Price-Whelan, A. M., Sipőcz, B. M., et al. 2018, AJ, 156, 123
Astropy Collaboration, Robitaille, T. P., Tollerud, E. J., et al. 2013, A&A, 558, A33
Bellm, E. C., Kulkarni, S. R., Graham, M. J., et al. 2019, PASP, 131, 018002
Bertin, E., & Arnouts, S. 1996, A&AS, 117, 393
Boyle, A., Sim, S. A., Hachinger, S., & Kerzendorf, W. 2017, A&A, 599, A46
Breeveld, A. A., Landsman, W., Holland, S. T., et al. 2011, in AIP Conf. Ser. 1358, ed. J. E. McEnery, J. L. Racusin, & N. Gehrels (Melville, NY: AIP), 373
Cardelli, J. A., Clayton, G. C., & Mathis, J. S. 1989, ApJ, 345, 245
Chambers, K. C., Magnier, E. A., Metcalfe, N., et al. 2016, arXiv:1612.05560
Chatzopoulos, E., Wheeler, J. C., Vinko, J., Horvath, Z. L., & Nagy, A. 2013, ApJ, 773, 76
Chen, P., Dong, S., Stritzinger, M. D., et al. 2020, ApJL, 889, L6
Chen, T. W., Yang, S., Pan, Y. C., et al. 2021, TNSAN, 92, 1
Das, K. K., Fremling, C., Kasliwal, M. M., et al. 2024, ApJL, 969, L11
De, K., Kasliwal, M. M., Ofek, E. O., et al. 2018, Sci, 362, 201
Dessart, L., Hillier, D. J., Li, C., & Woosley, S. 2012, MNRAS, 424, 2139
Drout, M. R., Soderberg, A. M., Gal-Yam, A., et al. 2011, ApJ, 741, 97
Drout, M. R., Soderberg, A. M., Mazzali, P. A., et al. 2013, ApJ, 774, 58
Eldridge, J. J., Stanway, E. R., Xiao, L., et al. 2017, PASA, 34, e058
Frohmaier, C., Angus, C. R., Vincenzi, M., et al. 2021, MNRAS, 500, 5142
Fulton, M., Moore, T., Srivastav, S., et al. 2023, TNSAN, 339, 1
Gehrels, N. 1986, ApJ, 303, 336
Gehrels, N., Chincarini, G., Giommi, P., et al. 2004, ApJ, 611, 1005
Gillanders, J. H., Huber, M., Chambers, K., et al. 2023, TNSAN, 341, 1
Gillanders, J. H., Sim, S. A., & Smartt, S. J. 2020, MNRAS, 497, 246
Gomez, S., Berger, E., Nicholl, M., Blanchard, P. K., & Hosseinzadeh, G. 2022, ApJ, 941, 107
Guillochon, J., Nicholl, M., Villar, V. A., et al. 2018, ApJS, 236, 6
Güver, T., & Özel, F. 2009, MNRAS, 400, 2050
Harris, C. R., Millman, K. J., van der Walt, S. J., et al. 2020, Natur, 585, 357
Ho, A. Y. Q., Perley, D. A., Gal-Yam, A., et al. 2023, ApJ, 949, 120
Hunter, J. D. 2007, CSE, 9, 90
Inserra, C. 2019, NatAs, 3, 697
Jiang, B., Jiang, S., & Ashley Villar, V. 2020, RNAAS, 4, 16
Karambelkar, V., Andreoni, I., Sollerman, J., et al. 2023a, TNSAN, 335, 1
Karambelkar, V., Das, K., Lin, Z., et al. 2023b, TNSAN, 340, 1
Kasen, D., & Bildsten, L. 2010, ApJ, 717, 245
Kashiyama, K., Murase, K., Bartos, I., Kiuchi, K., & Margutti, R. 2016, ApJ, 818, 94
Kasliwal, M. M., Kulkarni, S. R., Gal-Yam, A., et al. 2010, ApJL, 723, L98
Katz, B., Kushnir, D., & Dong, S. 2013, arXiv:1301.6766
Kerzendorf, W. E., & Sim, S. A. 2014, MNRAS, 440, 387
Kroupa, P. 2001, MNRAS, 322, 231
Kuncarayakti, H., Sollerman, J., Izzo, L., et al. 2023
Labrie, K., Simpson, C., Cardenes, R., et al. 2023a, RNAAS, 7, 214
Labrie, K., Simpson, C., Turner, J., et al. 2023b, DRAGONS, v3.1.0, Zenodo, doi:10.5281/zenodo.7776065
Lee, M. H., Zeng, K. J., Chen, T. W., et al. 2023, TNSAN, 338, 1
Mazzali, P. A., Sullivan, M., Pian, E., Greiner, J., & Kann, D. A. 2016, MNRAS, 458, 3455
McBrien, O. 2021, PhD thesis, Queen's Univ. Belfast
Modjaz, M., Blondin, S., Kirshner, R. P., et al. 2014, AJ, 147, 99
Modjaz, M., Gutiérrez, C. P., & Arcavi, I. 2019, NatAs, 3, 717
Moe, M., & Di Stefano, R. 2017, ApJS, 230, 15
Moore, T., Smartt, S. J., Nicholl, M., et al. 2023, ApJL, 956, L31
Moriya, T. J., Mazzali, P. A., Tominaga, N., et al. 2017, MNRAS, 466, 2085
Nadyozhin, D. K. 1994, ApJS, 92, 527
Nagao, T., Kuncarayakti, H., Maeda, K., et al. 2023, A&A, 673, A27
Nicholl, M. 2018a, RNAAS, 2, 230
Nicholl, M., Guillochon, J., & Berger, E. 2017, ApJ, 850, 55
Nicholl, M., Srivastav, S., Fulton, M. D., et al. 2023, ApJL, 954, L28
Perley, D. A., Sollerman, J., Schulze, S., et al. 2022, ApJ, 927, 180
Piro, A. L., Haynie, A., & Yao, Y. 2021, ApJ, 909, 209
Poole, T. S., Breeveld, A. A., Page, M. J., et al. 2008, MNRAS, 383, 627
Poznanski, D., Chornock, R., Nugent, P. E., et al. 2010, Sci, 327, 58
Poznanski, D., Prochaska, J. X., & Bloom, J. S. 2012, MNRAS, 426, 1465
Prentice, S. J., Maguire, K., Flörs, A., et al. 2020, A&A, 635, A186
Prentice, S. J., Maguire, K., Smartt, S. J., et al. 2018, ApJL, 865, L3
Quimby, R. M., De Cia, A., Gal-Yam, A., et al. 2018, ApJ, 855, 2
Rodríguez, Ó., Maoz, D., & Nakar, E. 2023, ApJ, 955, 71
Roming, P. W. A., Kennedy, T. E., Mason, K. O., et al. 2005, SSRv, 120, 95
Sawada, R., Kashiyama, K., & Suwa, Y. 2022, ApJ, 927, 223
Schlafly, E. F., & Finkbeiner, D. P. 2011, ApJ, 737, 103
Shen, K. J., & Bildsten, L. 2009, ApJ, 699, 1365
Shen, K. J., Kasen, D., Weinberg, N. N., Bildsten, L., & Scannapieco, E. 2010, ApJ, 715, 767
Shingles, L., Smith, K. W., Young, D. R., et al. 2021, TNSAN, 7, 1
Sim, S. A., Fink, M., Kromer, M., et al. 2012, MNRAS, 420, 3003
Smith, K. W., Smartt, S. J., Young, D. R., et al. 2020, PASP, 132, 085002
Smith, K. W., Williams, R. D., Young, D. R., et al. 2019, RNAAS, 3, 26
Sollerman, J. 2023, TNSTR, 2023-3158, 1
Speagle, J. S. 2020, MNRAS, 493, 3132
Springob, C. M., Haynes, M. P., Giovanelli, R., & Kent, B. R. 2005, ApJS, 160, 149
Srivastav, S., Moore, T., Nicholl, M., et al. 2023, ApJL, 956, L34
Srivastav, S., Smartt, S. J., Huber, M. E., et al. 2022, MNRAS, 511, 2708
Stanway, E. R., & Eldridge, J. J. 2018, MNRAS, 479, 75
Steele, I. A., Smith, R. J., Rees, P. C., et al. 2004, Proc. SPIE, 5489, 679
Stehle, M., Mazzali, P. A., Benetti, S., & Hillebrandt, W. 2005, MNRAS, 360, 1231
Stevance, H., Eldridge, J., & Stanway, E. 2020, JOSS, 5, 1987
Stritzinger, M., Mazzali, P., Phillips, M. M., et al. 2009, ApJ, 696, 713
Stritzinger, M. D., Anderson, J. P., Contreras, C., et al. 2018, A&A, 609, A134
Thornton, I., Villar, V. A., Gomez, S., & Hosseinzadeh, G. 2023, AAS Meeting Abstracts, 55, 107.24
Tonry, J. L., Denneau, L., Heinze, A. N., et al. 2018, PASP, 130, 064505
Tully, R. B., Courtois, H. M., Dolphin, A. E., et al. 2013, AJ, 146, 86
Villar, V. A., Berger, E., Metzger, B. D., & Guillochon, J. 2017, ApJ, 849, 70
Wang, S. Q., Wang, L. J., Dai, Z. G., & Wu, X. F. 2015, ApJ, 799, 107
Wheeler, J. C., Johnson, V., & Clocchiatti, A. 2015, MNRAS, 450, 1295
Woosley, S. E. 2010, ApJL, 719, L204
Woosley, S. E., Pinto, P. A., & Hartmann, D. 1989, ApJ, 346, 395
Wu, S. C., & Fuller, J. 2022, ApJL, 940, L27
Wygoda, N., Elbaz, Y., & Katz, B. 2019, MNRAS, 484, 3941
Yan, S., Wang, X., Gao, X., et al. 2023, ApJL, 959, L32
Yao, Y., De, K., Kasliwal, M. M., et al. 2020, ApJ, 900, 46
Yaron, O., & Gal-Yam, A. 2012, PASP, 124, 668